https://doi.org/10.1016/j.atmosenv.2020.117362
This is the Pre-Published Version.

Simplified and Fast Atmospheric Radiative Transfer model for satellite-based aerosol optical depth retrieval

Xing Yan[1*], Nana Luo [2], Chen Liang [1], Zhou Zang [1], Wenji Zhao [3], Wenzhong Shi [4]

[1] State Key Laboratory of Remote Sensing Science, College of Global Change and Earth System Science, Beijing Normal University, Beijing 100875, China

[2] Department of Geography, San Diego State University, 5500 Campanile Dr., San Diego, CA 92182-4493, USA

[3] College of Resource Environment and Tourism, Capital Normal University, Beijing, 100048, China

[4] Department of Land Surveying and Geo-Informatics, The Hong Kong Polytechnic University, Hong Kong, China

*Corresponding author: Xing Yan (yanxing@bnu.edu.cn)

Abstract

Satellite-based aerosol optical depth (AOD) retrieval over land remains a considerable challenge when high temporal and spatial resolutions are required. This paper presents the Simplified and Fast Atmospheric Radiative Transfer (SFART) model for direct calculation of satellite AOD via analytical equations rather than the lookup table (LUT) approach. The SFART model considers the impact of both Rayleigh and aerosol multiple scattering. A comprehensive comparison with the Simplified Method for Atmospheric Correction (SMAC) and single scattering approximation method is conducted. In validation with 6S, good atmospheric reflectance (Rayleigh + aerosol) accuracy is achieved by SFART, with approximately 69% of the data falling within the 5% estimated error (EE) envelope at both 440 and 640 nm. This is higher than the SMAC accuracy (within 5% EE: 42.83% and 39.91% at 440 and 640 nm, respectively) and is a tremendous improvement over the single scattering approximation method (within 5% EE: 15.67% and 20.5% at 440 and 640 nm, respectively). SFART is then applied for AOD retrieval to Himawari-8 satellite data over the North China Plain on both normal and hazy days. The retrieved AOD values are validated against collected AERONET data (Version 3, Level 2.0). Approximately 59% of the SFART AOD values fall within the EE bounds of $\pm(0.05 + 15\%)$ with a root mean squared error of 0.22 (for 339 collocations). The promising results given by SFART indicate that this method can facilitate improved AOD calculation using empirical or real-time aerosol models in an efficient and flexible manner.

Keywords: AOD, Himawari-8, AERONET, SMAC

1 Introduction

Aerosols are suspensions of solid or liquid particulate matter in the atmosphere, which have significant influence on the Earth's energy budget (Bellouin et al., 2005), climate (Kaufman et al., 2002; Ramanathan et al., 2001), and human health (Anderson et al., 2012). Aerosols exhibit strong spatial and temporal variability in the atmospheric environment (Remer et al., 2005). Thus, accurate monitoring of aerosols with high temporal resolution and on regional or global scales is necessary. In the context of aerosol monitoring, the aerosol optical depth (AOD) is one of the most common aerosol products retrieved by satellites. The AOD describes the magnitude of the solar-light attenuation due to aerosols. Satellites produce large-scale AOD images, allowing resolution of the spatial patterns resulting from different aerosol sources (Li et al., 2009). Furthermore, as air pollution is currently a significant issue throughout the world, AOD retrieval is attracting increased attention (Bi et a., 2019; Li et al., 2018; Xin et al., 2016).

Various algorithms for satellite AOD retrieval have been developed in recent years, for which use of a lookup table (LUT) is one of the most widely employed techniques. Through use of accurate but complex radiative transfer models (RTMs) such as Second Simulation of a Satellite Signal in the Solar Spectrum (6S; Vermote et al., 2006), Santa Barbara DISORT Atmospheric Radiative Transfer (SBDART, where DISORT represents "discrete-ordinate-method radiative transfer"; Ricchiazzi et al., 1998), SCIATRAN (Rozanov et al., 2005), and Moderate Resolution Atmospheric Transmission (MODTRAN; Berk et al., 1987), an LUT is generated and employed for fast calculation of the AOD from the satellite data (Zha et al., 2011). For example, the Moderate Resolution Imaging Spectrometer (MODIS) Dark Target (DT) algorithm applies a 6S-based LUT for AOD retrieval at 10- and 3-km spatial resolutions (Levy et al., 2007; Munchak et al., 2013). Similarly, MODIS AOD retrieval with 1-km spatial resolution is achieved via the Multiangle Implementation of Atmospheric Correction (MAIAC) method

(Lyapustin et al., 2011a, b), with an LUT based on the Spherical Harmonics (SHARM) code being used to calculate the AOD (Lyapustin, 2005).

The LUT technique is popular for satellite AOD retrieval because the general RTM calculations are time-consuming, especially for high-spatial-resolution and large-scale-coverage satellite sensors (Katsev et al., 2009). However, LUT-based AOD has some inherent limitations. First, the LUT is generated by the specific aerosol model, but must be recomputed every time the aerosol model is changed. Second, the LUT size can impact the final result. To date, no reasonable LUT size with appropriate angle or AOD intervals has been determined. Previously, Lee et al. (2015) reported that the accuracy of an LUT built according to a 5° solar zenith angle (SZA) interval was much higher than that of an LUT constructed with 10° intervals under high SZA conditions (approximately 60°). Currently, the DT LUT is generated with a 6° SZA interval (Levy et al., 2007). However, the MAIAC algorithm employs an interval of approximately 2.87° to construct the LUT (Lyapustin et al., 2018).

To overcome these limitations of the LUT technique, some researchers have developed modified RTMs for direct calculation of satellite AOD. The merits of this approach are its minimal complexity and high computation speed, and that the final AOD result can be obtained using flexible aerosol models. In these modified RTMs, the approximate analytical equations are simplified, especially those for atmospheric reflectance calculation (Rayleigh reflectance + aerosol reflectance). Some simplified RTMs employ single scattering for the atmospheric reflectance approximation (a summary is presented in Table 1). For example, Riffler et al. (2010) have developed a modified Advanced Very High Resolution Radiometer (AVHRR) aerosol optical depth retrieval algorithm, which employs only the single scattering approximation for Rayleigh and aerosol reflectance calculation. This single scattering approximation is also used in

the Simplified High-resolution Aerosol Retrieval Algorithm (SARA; Bilal et al., 2013) and the Simplified Atmospheric Correction Algorithm for Chinese Gaofen (SAHARA; She et al., 2017).

Table 1. Literature summary of simplified RTMs

Method	Rayleigh reflectance	Aerosol reflectance	Reference
SMAC	Single scattering approximation	Multiple scattering approximation	Rahman and Dedieu (1994)
Modified AVHRR AOD retrieval algorithm	Single scattering approximation	Single scattering approximation	Riffler et al. (2010)
SMART	Multiple scattering approximation	Multiple scattering approximation	Seidel et al. (2010)
SARA	Single scattering approximation	Single scattering approximation	Bilal et al. (2013)
A AVHRR AOD retrieval algorithm	Single scattering approximation	Multiple scattering approximation	Mei et al. (2014)
SAHARA	Single scattering approximation	Single scattering approximation	She et al. (2017)
MAARM	Single scattering approximation	Multiple scattering approximation	Yan et al. (2018)

Although use of the single scattering approximation allows extremely fast RTM computation, Antoine and Morel (1998) have noted significant differences between single and multiple scattering approximations for aerosol reflectance calculation. Thus, some researchers have considered the impact of multiple scattering when developing RTMs. Among them, Seidel et al. (2010) have developed the Simple Model for Atmospheric Radiative Transfer (SMART), which has been tested on airborne AOD retrieval (Seidel et al., 2012). However, the SMART accuracy assessment was only conducted for an AOD range of 0–0.5 (Seidel et al., 2010), whereas the general range of satellite-based AOD is 0–2 (Kokhanovsky et al., 2005). In addition,

Rahman et al. (1994) have developed the Simplified Method for Atmospheric Correction (SMAC), which is an empirically based simplification of the Simulation of Satellite Signals in the Solar Spectrum (5S) code. Although SMAC is up to 3000 times faster than 6SV1.1, Proud et al. (2010) have shown that good accuracy is only obtained at low viewing and solar angles (< 30°). Finally, Yan et al. (2018) have proposed the Minimum Albedo Aerosol Retrieval Method (MAARM) for the Himawari-8 satellite, which considers the impact of aerosol multiple scattering; however, this method also uses the single scattering approximation for Rayleigh reflectance calculation. Thus, the accuracies of simplified RTMs for satellite AOD retrieval incorporating approximations of multiple scattering for both Rayleigh and aerosol reflectance remain limited.

In this study, the newly developed Simplified and Fast Atmospheric Radiative Transfer (SFART) model is presented, which integrates SMAC and the Successive Order of Scattering (SOS) method. Rather than LUTs, SFART uses analytical equations for satellite AOD retrieval. This approach has the following advantages: it considers the impact of multiple scattering for both Rayleigh and aerosol reflectance which allowing fast calculation, and can take empirical or real-time ground-based measured aerosol model information as input. Thus, SFART is much more convenient and flexible than LUT-based methods.

2 SFART algorithm

2.1 Radiative transfer equation

Based on the total gas absorption correction, the corrected reflectance (ρ_λ) measured by a satellite can be estimated (Vermote et al., 1997) from the relation

$$\rho_{\lambda}=\rho^{a}+\frac{T_{(\theta_0)}T_{(\theta)}}{1-\rho_s S_{(\lambda)}}\rho_s, \quad (1)$$

where θ_0 is the solar zenith angle; θ is the satellite zenith angle; ρ^a is the atmospheric reflectance; ρ_s is the surface reflectance; $T_{(\theta_0)}$ and $T_{(\theta)}$ are the downward and upward total scattering transmittances, respectively; and $S_{(\lambda)}$ is the atmospheric backscattering ratio. Here, ρ^a represents the combination of Rayleigh reflectance ρ_{Ray} and aerosol reflectance ρ_{Aer} (the scattering interaction between molecules and aerosols is neglected in this study), and can therefore be expressed as

$$\rho^{a}=\rho_{Aer}+\rho_{Ray}. \quad (2)$$

2.2 Rayleigh atmospheric reflectance

In the proposed SFART model, the contribution of molecular (Rayleigh) scattering is incorporated by considering multiple scattering (Vermote and Tanre, 1992):

$$\rho_{Ray}=\overbrace{\sum_{m=0}^{2}(2-\delta_{0,m})\times\rho_1^m(\mu_s,\mu_v,\phi-\phi_0)\times\cos[m(\phi-\phi_0)]}^{\text{Single scattering contribution}}+\underbrace{(1-\mathrm{e}^{-\tau/\mu_s})\times(1-\mathrm{e}^{-\tau/\mu_v})\times\sum_{m=0}^{2}(2-\delta_{0,m})\times\Delta^m(\tau_R)\times\mathrm{P}^m(\mu_s,\mu_v)\times\cos[m(\phi-\phi_0)]}_{\text{Higher orders of scattering}}, \quad (3)$$

where μ_s is the cosine of the solar zenith angle; μ_v is the cosine of the sensor zenith angle; $\phi-\phi_0$ is the relative azimuth angle between the viewing ϕ and solar direction ϕ_0 angles; $\delta_{0,m}$ is the Kronecker symbol; and $\Delta^m(\tau_R)$ is a function having a complementary angular dependence, the

details of which can be found in Vermote and Tanre (1992). Further, ρ_1^m is the single scattering reflectance corresponding to the *m* term of the phase function (*m* = 0,1,2), such that

$$\rho_1^m(\mu_s,\mu_v) = \mathrm{P}^m \times (1-\mathrm{e}^{-\tau_R(1/\mu_s+1/\mu_v)}) \times \frac{1}{4(\mu_s+\mu_v)}. \quad (4)$$

Here, τ_R is the Rayleigh optical thickness and P^m is the Fourier series expansion of the Rayleigh phase function:

$$\begin{cases} \mathrm{P}^0 = 1+\dfrac{1}{8}\times(3\mu_v-1)^2\times(3\mu_s-1)^2\times\dfrac{1-\dfrac{\delta}{2-\delta}}{1+2\times\dfrac{\delta}{2-\delta}} \\ \mathrm{P}^1 = -1.5\times\dfrac{1}{2}\times\mu_s\mu_v\times\sqrt{1-\mu_s^{\,2}}\times\sqrt{1-\mu_v^{\,2}}\times\dfrac{1-\dfrac{\delta}{2-\delta}}{1+2\times\dfrac{\delta}{2-\delta}}, \\ \mathrm{P}^2 = 0.375\times\dfrac{1}{2}\times(1-\mu_s^{\,2})\times(1-\mu_v^{\,2})\times\dfrac{1-\dfrac{\delta}{2-\delta}}{1+2\times\dfrac{\delta}{2-\delta}} \end{cases} \quad (5)$$

where δ = 0.0279 is the depolarization factor (Young, 1980).

2.3 Aerosol atmospheric reflectance

The ρ_{Aer} considered in this study also incorporates the multiple scattering contribution. When θ_0 or $\theta < 30°$, ρ_{Aer} is expressed as follows (Rahman and Dedieu, 1994):

$$\rho_{Aer} = \frac{1}{\mu_s \mu_v}\left\{\frac{X\mu_v}{1+k\mu_v}(1-\exp(-\tau_a(1+k\mu_v)/\mu_v))\right.$$
$$+\frac{Y\mu_v}{1+k\mu_v}(1-\exp(-\tau_a(1-k\mu_v)/\mu_v)) \quad , \quad (6)$$
$$\left.+[Z+P_t(\Theta_t)]\frac{\mu_s\mu_v}{\mu_s+\mu_v}(1-\exp(-\tau_a(1/\mu_s+1/\mu_v)))\right\}$$

with $k^2=(1-\omega_0)(3-3\omega_0 g)$; where τ_a is the AOD; ω_0 is the single scattering albedo (SSA); g is the asymmetry factor; and X, Y, and Z are complex functions of ω_0, g, μ_s, and μ_v, which are presented in the Supplementary Materials. Furthermore, $P_t(\Theta_t)$ is the Henyey-Greenstein phase function, which depends on the scattering angle Θ_t:

$$P_t(\Theta_t)=\frac{1-g^2}{[1+g^2-2g\cos(\Theta_t)]^{1.5}}, \quad (7)$$

where (Rahman and Dedieu, 1994)

$$\Theta_t=\cos^{-1}(-\cos(\theta_0)\cos(\theta)+\sin(\theta_0)\sin(\theta)\cos(\phi-\phi_0)). \quad (8)$$

When θ_0 or $\theta \geq 30°$, ρ_{Aer} is determined via a modified second-order SOS method. Then,

$$\rho_{Aer}(\mu_v,\mu_s,\phi-\phi_0)=R^{\mathrm{I}}(\mu_v,\mu_s,\phi-\phi_0)+R^{\mathrm{II}}(\mu_v,\mu_s,\phi-\phi_0), \quad (9)$$

where R^{I} is the first-order aerosol scattering (Hansen & Travis, 1974):

$$R^{\mathrm{I}}(\mu_v,\mu_s,\phi-\phi_0)=\frac{\omega_0 P_r(\mu_v,\mu_s,\phi-\phi_0)}{4(\mu_s+\mu_v)}\left\{1-\exp[-\tau_a(\frac{1}{\mu_v}+\frac{1}{\mu_s})]\right\}. \quad (10)$$

Note that P_r is the modified Henyey-Greenstein function, which moderates the overall contributions of the forward and backward scattering and is defined as (Rahman et al., 1993)

$$P_r(\mu_v,\mu_s,\phi-\phi_0)=\frac{1-g^2}{[1+g^2-2g\cos(\pi-\xi)]^{1.5}}. \quad (11)$$

The phase angle ξ is given by

$$\begin{aligned}\cos(\xi) &= \cos(\theta_0)\cos(\theta) + \sin(\theta_0)\sin(\theta)\cos(\phi - \phi_0) \\ &= \mu_0\mu + \sqrt{(1-\mu_s^2)(1-\mu_v^2)}\cos(\phi - \phi_0)\end{aligned} . \quad (12)$$

The second-order scattering R^{II} is a modification of Hansen and Travis (1974):

$$\begin{aligned}R^{\mathrm{II}}(\mu_v, \mu_s, \phi - \phi_0) = \frac{\mu_v^2 + \mu_s^2}{\mu_v + \mu_s} \times \frac{\tau_a \omega_0}{4\pi} \int_0^{2\pi}\int_0^1 [&\frac{1}{\mu_v} P_t(\mu_v, \mu_v', \phi - \phi') R^{\mathrm{I}}(\mu_v', \mu_s, \phi' - \phi_0) \\ &+ \frac{1}{\mu_s} R^{\mathrm{I}}(\mu_v, \mu_v', \phi - \phi') P_t(\mu', \mu_s, \phi' - \phi_0) \\ &- \frac{e^{\frac{-\tau_a}{\mu_s}}}{\mu_s} T(\mu_v, \mu_v', \phi - \phi') P_r(\mu_v', \mu_s, \phi' - \phi_0) \\ &- \frac{e^{\frac{-\tau_a}{\mu_v}}}{\mu_v} P_r(\mu_v, \mu_v', \phi - \phi') T(\mu_v', \mu_s, \phi' - \phi_0)] d\mu_v' d\phi'\end{aligned} . (13)$$

Here, P_t is the Henyey-Greenstein phase function mentioned above, which depends on Θ_t.

Finally, T is the single scattering transmittance, given by

$$T(\mu_v, \mu_s, \phi - \phi_0) = \frac{\omega_0 P_t(\Theta_t)}{4(\mu_v - \mu_s)}[\exp(\frac{-\tau_a}{\mu_v}) - \exp(\frac{-\tau_a}{\mu_s})] . \quad (14)$$

From l' Hospital's rule, for $\mu = \mu_0$,

$$T(\mu_s, \mu_s, \phi - \phi_0) = \frac{\omega_0 \tau_a}{4\mu_s^2}\exp(\frac{-\tau_a}{\mu_s}) P_t(\Theta_t) . \quad (15)$$

2.4 Application of SFART for satellite AOD retrieval

Japan's new-generation geostationary meteorological satellite sensor, Himawari-8, was launched on 7 October 2014, and began to provide image data on 7 July 2015 (Bessho et al., 2016). Himawari-8 is capable of monitoring aerosol variations at a high temporal resolution of 10 min. Thus, in this study, we used Himawari-8 image data to test the SFART performance.

Daytime 2:00 (coordinated universal time, UTC) Himawari L1 gridded data with 5-km spatial resolution were obtained for the full year of 2018 from the Japanese Aerospace Exploration Agency Earth Observation Research Center (ftp.ptree.jaxa.jp). We used the Band-1 (blue, 470 nm) and Band-3 (red, 640 nm) data as the SFART input data for AOD calculation. A flowchart describing SFART application for Himawari-8 AOD retrieval is shown in Figure 1.

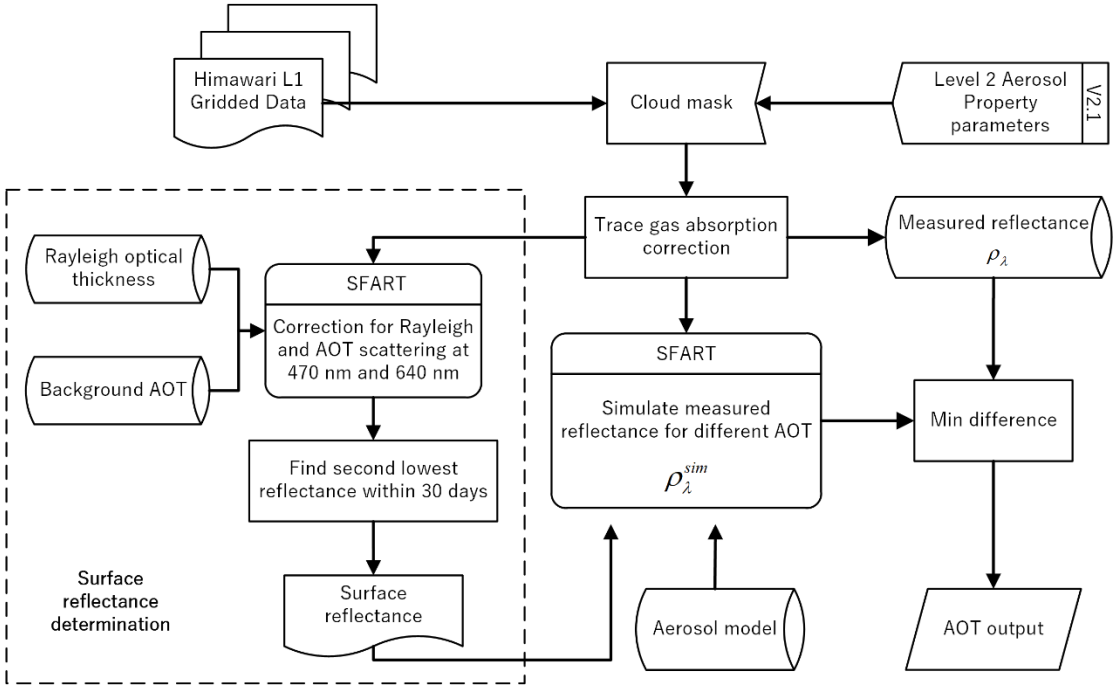

Figure 1. Flowchart showing SFART application for Himawari-8 AOD retrieval

The cloud mask used in this study was based on the Himawari-8 Cloud Property dataset (V2.1), which provides cloud flag information (details are available at https://www.eorc.jaxa.jp/ptree/userguide.html). It should be noted that the Himawari-8 Cloud Property dataset does not provide the ice cloud properties information, but this work has been investigated in Letu et al. (2018). Then, the measured reflectance obtained from the Himawari L1 gridded data (ρ_λ^{L1}) was corrected for the trace gas absorption (Patadia et al., 2018):

$$\rho_\lambda = \tilde{T}_\lambda^{gas} \rho_\lambda^{L1}, \quad (16)$$

where $\tilde{T}_\lambda^{gas}$ is the product of individual gas corrections that can be found in Patadia et al. (2018).

In this study, we assumed that ρ_s was Lambertian. This initial assumption is employed in many approaches, such as 6S (Vermote et al., 2006) and the synergy-based AOD retrieval algorithm (Shi et al., 2017). For the ρ_s determination, we used the reflectance corrected for Rayleigh and background AOD (τ_B) scattering at the 470- and 640-nm bands having the second-lowest reflectance within 30 days. We applied SFART to achieve this work in a pixel-by-pixel manner. Here, ρ_s was obtained from the relation

$$\rho_s = \min^{2nd}\left(\frac{\rho_\lambda - \rho_{Ray}(\tau_R) - \rho_{Aer}(\tau_B)}{T_{(\theta_0)}T_{(\theta)} + S[\rho_\lambda - \rho_{Ray}(\tau_R) - \rho_{Aer}(\tau_B)]}\right). \quad (17)$$

The atmospheric spherical albedo (S) and total atmospheric transmission (T) in SFART are identical to those of SMAC (Rahman et al., 1994). Proud et al. (2010) have confirmed that the SMAC S and T have good accuracy in comparison with 6S. In this study, we adopted the aerosol model given by Lee and Kim (2010). In the case of hazy conditions, we directly employed real-time Aerosol Robotic Network (AERONET) aerosol model data (ω_0 and g). Finally, the simulated measured reflectance (ρ_λ^{sim}) given by SFART was determined from the relation

$$\begin{aligned}\rho_\lambda^{sim} = {} & \rho_{Ray}\big|multiple \\ & + \rho_{Aer}\big|multiple \begin{cases} SMAC \ \ (\theta_0 \ and \ \theta < 30°) \\ Second \ \ order \ \ SOS \ \ (\theta_0 \ or \ \theta \geq 30°) \end{cases} \\ & + \frac{T_{(\theta_0)}T_{(\theta)}}{1-\rho_s S_{(\lambda)}}\rho_s \Big| \min^{2nd} \rho_s \ corrected \ by \ \tau_R, \tau_B \end{aligned}. \quad (18)$$

The difference between ρ_λ^{sim} and ρ_λ was calculated as follows:

$$\begin{cases} \rho_{470nm}^{sim} - \rho_{470nm} = 0 \\ ABS(\rho_{640nm}^{sim} - \rho_{640nm}) / \rho_{640nm} = \varepsilon . \\ \tau_a^{470nm} > \tau_a^{640nm} \end{cases} \quad (19)$$

The final AOD outputs at 470 and 640 nm were determined through solution of Eq. (19), for which the fitting error ε at 640 nm was minimized. Then, the 500-nm AOD was interpolated from the 470- and 640-nm AOD for comparison with Himawari-8 (V2.1) aerosol products.

3 Results and discussion

3.1 Comparison of derived Rayleigh reflectance

As shown in Eq. (2), ρ^a is a combination of ρ_{Ray} and ρ_{Aer}. Although many studies have employed single approximation for ρ_{Ray} in the aerosol retrieval process (Riffler et al., 2010; Bilal et al., 2013; Shi et al., 2017), Yan et al. (2018) have shown that single-approximated Rayleigh reflectance is underestimated for both blue and red bands, especially in the short-wavelength blue band. This is because the Rayleigh optical thickness in the blue band τ_R^{Blue} is almost four times higher than that of the red band τ_R^{Red} for satellite sensors. For example, for MODIS, τ_R^{Blue} is 0.192 but τ_R^{Red} is 0.0508, and for the Visible Infrared Imaging Radiometer Suite (VIIRS), τ_R^{Blue} is 0.16 but τ_R^{Red} is 0.044 (Patadia et al., 2018). The difference between single and multiple scattering approximations of ρ_{Ray} (i.e., ρ_{Ray}^{Single} and ρ_{Ray}^{SFART}, respectively) in the blue band is presented in Figure 2 (the equation used for the ρ_{Ray} single approximation is given in the Supplementary Materials). Figure 2 was generated from 10,000 groups of uniformly distributed random satellite angles (θ_0 and θ: 0–60°, ϕ and ϕ_0: 0–180°). Although the absolute error of

ρ_{Ray}^{Single} and ρ_{Ray}^{SFART} (ABS) is small in most cases (<0.005), it increases significantly to more than 0.02 at large Θ_t, θ_0, and θ. In addition, under conditions of large θ_0 and θ (50–60°), and large Θ_t (140–180°), the error of the blue-band ρ_{Ray}^{Single} is always above 0.01. Previously, Gordon and Morel (1983) revealed that the Rayleigh reflectance is the main contributor to the satellite visible bands in the case of clear atmospheric conditions. To analyze the impact of the single-approximated Rayleigh reflectance on AOD retrieval, box plots of absolute errors of AOD (ρ_{Ray}^{Single} AOD - ρ_{Ray}^{SFART} AOD) as a function of absolute errors between ρ_{Ray}^{Single} and ρ_{Ray}^{SFART} were generated, as shown in Figure 2B. The AOD error increases as the error in Rayleigh reflectance increases. As shown in Figure 2B, when the absolute error of ρ_{Ray}^{Single} and ρ_{Ray}^{SFART} is larger than 0.012, the absolute error of the AOD result is always larger than 0.1 and the maximum absolute error can reach higher than 0.2. According to Figure 2, we conclude that a high ρ_{Ray}^{Single} error could yield serious uncertainties in the retrieved AOD values. Thus, multiple scattering for ρ_{Ray} approximation in satellite AOD retrieval should not be neglected, especially for the satellite blue band.

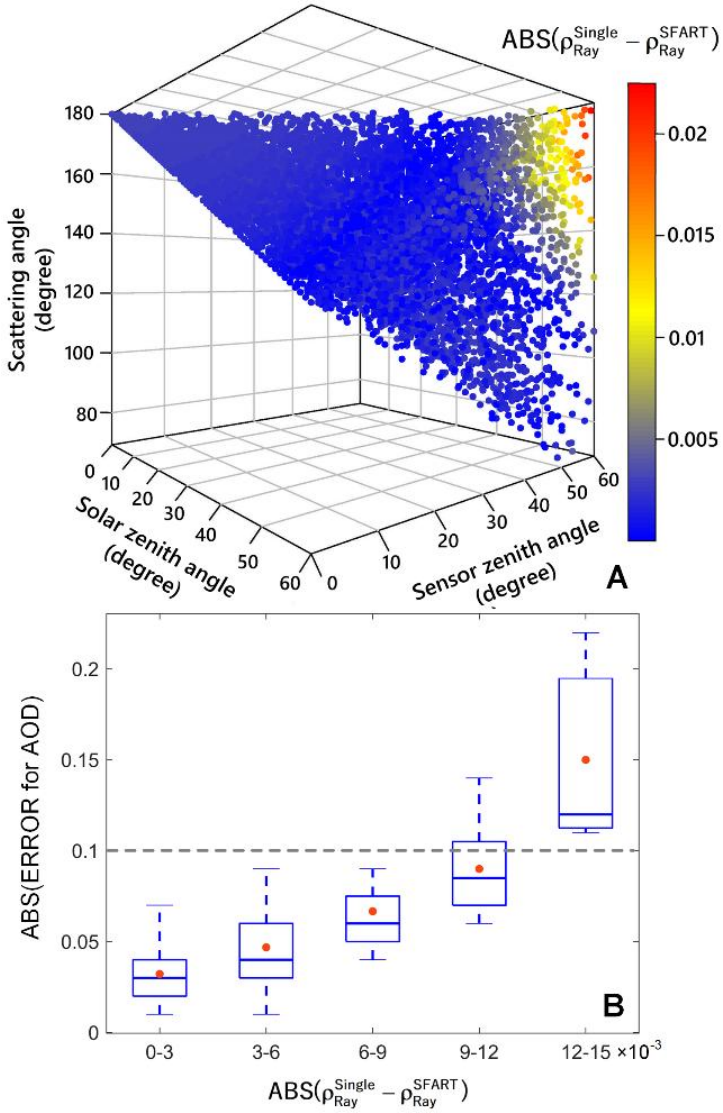

250

251 **Figure 2.** A: Plots of absolute errors between ρ_{Ray}^{Single} and ρ_{Ray}^{SFART} for various process variables. B:

252 Box plots of absolute errors ρ_{Ray}^{Single} AOD - ρ_{Ray}^{SFART} AOD as a function of the absolute error of ..-

253 ρ_{Ray}^{SFART}. The means, medians, and 66% intervals of the differences are shown as red dots,

254 horizontal blue lines within the boxes, and the boxes themselves, respectively. The blue whiskers

255 are the 96% intervals.

256

3.2 Comparing aerosol reflectance approximation

To test the performance of the aerosol reflectance approximation, we created 10,000 random data groups having θ_0 and θ of 0–60°, ϕ and ϕ_0 of 0–180°, and τ_a of 0–3, and used these groups as input data for SFART, SMAC, 6S, and a single-approximation RTM at 470 and 640 nm. For this part of the study, the 6S continental aerosol model was used to calculate the aerosol reflectance for comparison purpose. The ω_0 and g values at different wavelengths can be found in Tomasi et al. (2017). Comparison plots of ρ_{Aer} at 470 and 640 nm are provided in Figure 3. In the top-row plots (Figures 3 A and D), 68% of the SFART ρ_{Aer} values fall within the ±10% estimated error (EE) envelope at both 470 and 640 nm, and the high kernel density values indicate that most of the data lie close to the 1:1 line. However, in Figures 3 B and E, approximately 40% and 38% of the SMAC ρ_{Aer} points fall within the ±10% EE envelope for 470 and 640 nm respectively, which is much lower than the SFART ρ_{Aer} values. In addition, 45% (470 nm) and 43% (640 nm) of the SMAC-derived values are above the upper limit of the EE envelope. Data with high kernel density values are also above the 1:1 line. These results indicate that the SMAC ρ_{Aer} is overestimated in most cases. For the single-approximation ρ_{Aer} (Figures 3 C and F), only 14% (470 nm) and 13% (640 nm) of the results fall within the EE envelope, indicating significant differences between the single approximation and 6S results for the aerosol reflectance. Furthermore, for the case where only the single scattering impacts were considered (Figures 3 C and F), most of the data points in the figures are below the lower limit of the EE envelope (79% and 83% for 440 and 640 nm, respectively).

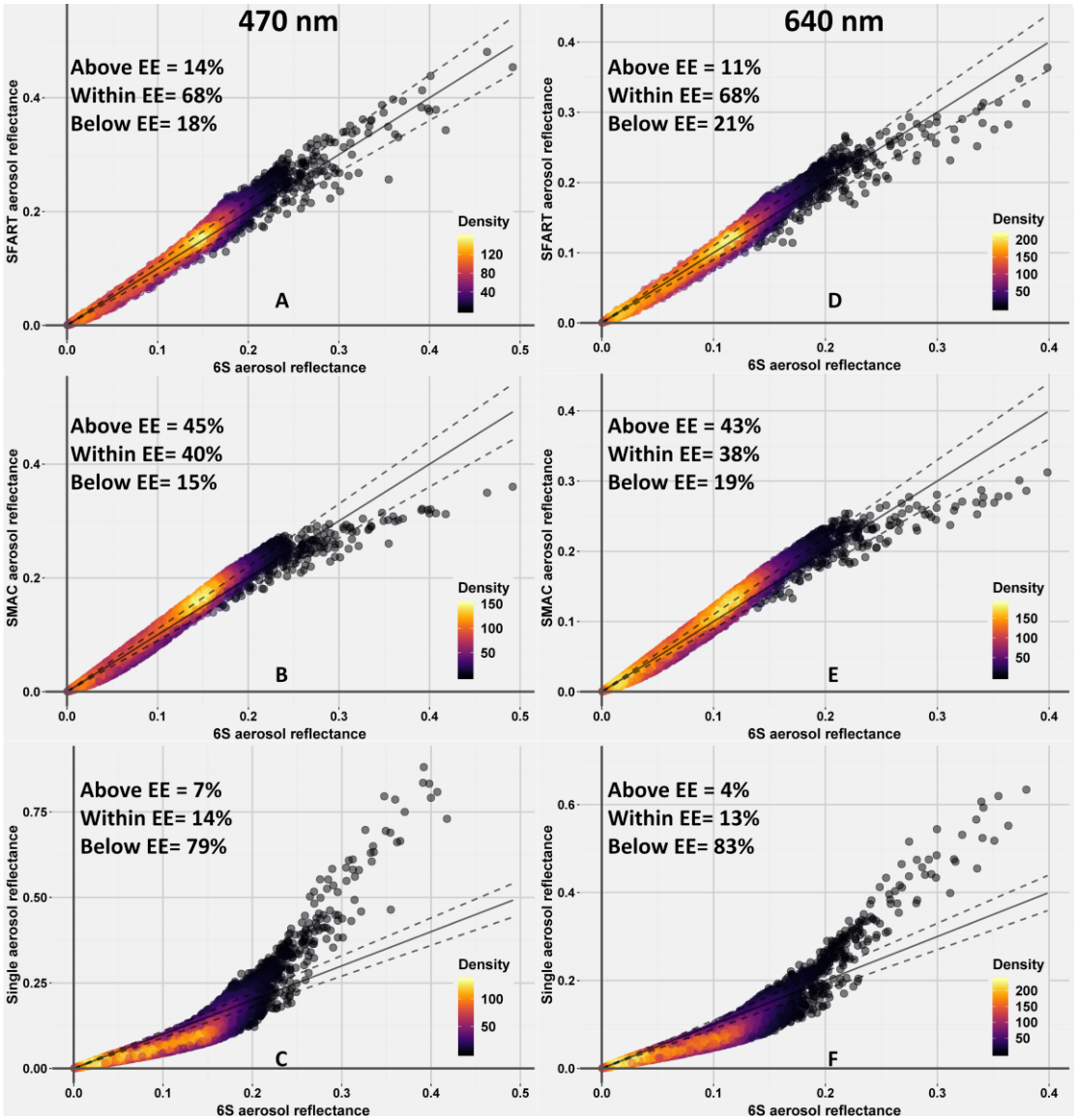

277

278 **Figure 3.** Density plots of aerosol reflectance computed by SFART, SMAC, single-
279 approximation RTM, and 6S for various process variables. The two dashed black lines are the
280 EE envelope lines, which are equal to ±10% × 6S aerosol reflectance. The solid black line is the
281 1:1 line.

282

3.3 Combination of Rayleigh and aerosol reflectance

A comparison of the total atmospheric reflectance (Rayleigh + aerosol reflectance) obtained for SFART, the single-approximation RTM, and SMAC with 6S is shown in Figure 4. Table 2 presents the statistical information corresponding to the comparison. Compared to SMAC, the SFART atmospheric reflectance results are much closer to the 1:1 line at both 470 and 640 nm. In detail, 69.26% and 68.55% of the SFART retrievals at 440 and 640 nm lie within the 5% EE, which is better than the SMAC results (42.83% and 39.91% at 440 and 640 nm, respectively, within 5% EE). In addition, the SMAC results indicate serious overestimation, with 42.04% and 48.30% of the results for 440 and 640 nm, respectively, falling above the 5% EE. However, SFART exhibits a significant improvement with regard to this overestimation, with only 19.06% (440 nm) and 21.82% (640 nm) of the data falling above the 5% EE. As regards the single-approximation results shown in Figure 4, there is significant deviation from the 1:1 line for both 440 and 640 nm. Only 15.67% and 20.5% of the retrievals fall within the 5% EE for 440 and 640 nm, respectively, and most of the retrievals are below the 5% EE (Table 2). In general, SFART yielded an error with much less bias than SMAC, which provided the best matches to 6S. In contrast, as apparent from Figure 4 and Table 2, high uncertainties were found for the single approximation, with most of the data being underestimated compared with 6S (76.98% and 75.12% below 5% EE for 440 and 640 nm, respectively). To analyze the impact of the errors of SFART-based total atmospheric reflectance (Rayleigh + aerosol reflectance) on the AOD retrieval, box plots of absolute errors of AOD (SFART AOD – 6S AOD) as a function of absolute errors of total atmospheric reflectance between SFART and 6S were prepared, as shown in Figure S1. When the absolute errors of the total atmospheric reflectance is small (<0.005), the error of the derived AOD is always below 0.1. Figure S1 also clearly presents that the derived

AOD error increases as the error in the total atmospheric reflectance increases. When the absolute errors of the total atmospheric reflectance is 0.02–0.025, the error of the derived AOD may exceed 0.4.

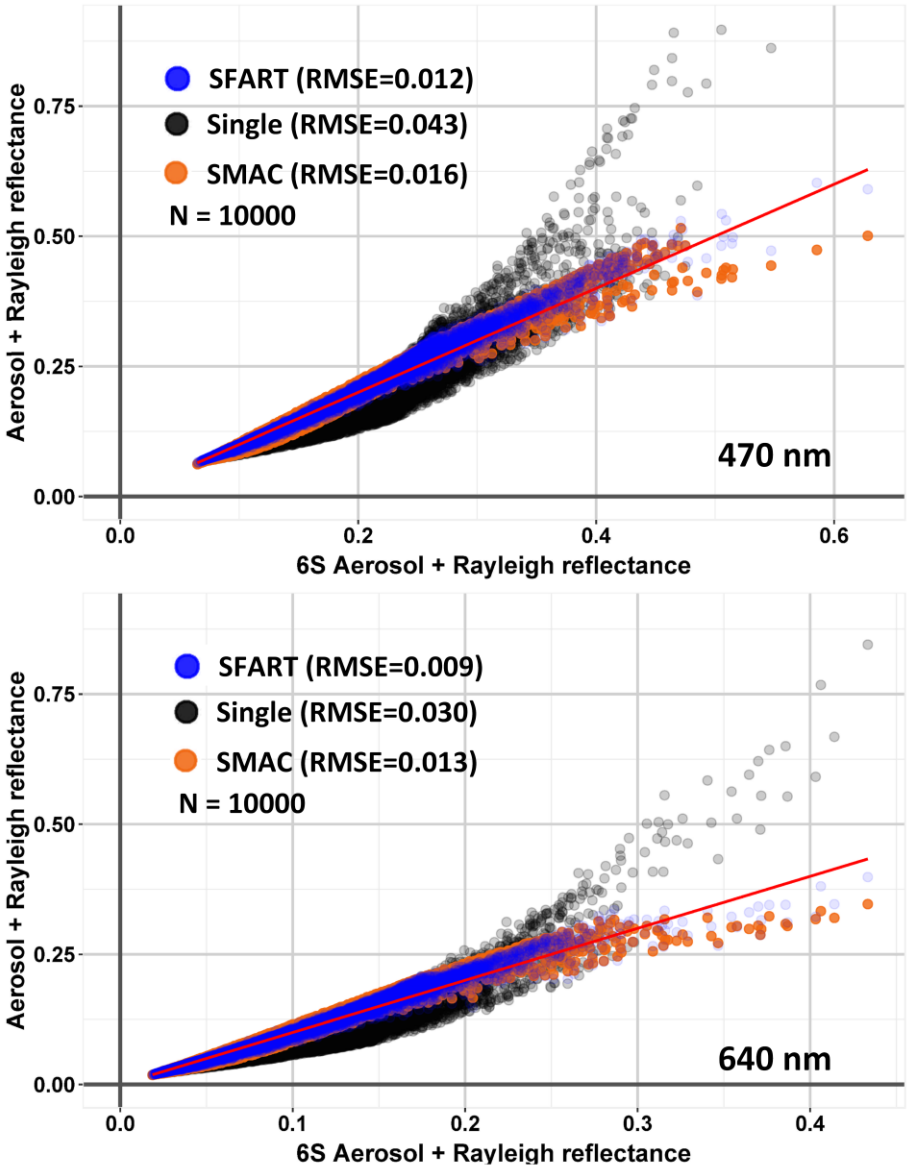

Figure 4. Aerosol + Rayleigh reflectance results computed by SFART, SMAC, single-approximation RTM, and 6S for various process variables. The red line is the 1:1 line.

Table 2. Statistics of the atmospheric reflectance comparison for SFART, SMAC and Single Approximation with 6S

Wavelength	RTM	N	RMSE	Within 5%EE	Above 5%EE	Below 5%EE
440 nm	SFART	10,000	0.012	69.26%	19.06%	11.68%
	SMAC	10,000	0.016	42.83%	42.04%	15.13%
	Single Approximation	10,000	0.043	15.67%	7.35%	76.98%
640 nm	SFART	10,000	0.009	68.55%	21.82%	9.63%
	SMAC	10,000	0.013	39.91%	48.30%	11.79%
	Single Approximation	10,000	0.030	20.5%	4.38%	75.12%

3.4 Comparison of SFART and SMAC for AOD retrieval

SFART was validated through comparison with the single approximation and SMAC, by comparing the derived AOD values with equivalent results from 6S. All RTMs were implemented under the random geometric condition (θ_0 = 0°–70°, θ = 0°–70°, ϕ = 0°–180°, ϕ_0 = 0°–180°), surface reflectance (0–0.2), and top of the atmosphere (TOA, 0.1–0.5), to facilitate a fair comparison. Figure 5A, B and C plot the retrieved AOD at 470 nm given by Single approximation, SMAC, and SFART. In this figure, 85% of the SFART AOD values fall within an EE of $\pm(0.05+15\%)$, which is a 23% increase over that of SMAC (62% within this EE) and a 55% increase over that of the Single approximation (30% within this EE). Overestimation and underestimation could also be improved, with fewer data points falling above or below the EE.

The histogram of the derived AOD errors with 6S for these three RTMs is shown in Figure 5D. Many of the AOD values are overestimated by the single approximation. This phenomenon is also revealed in Figure 5A, where 60% of single approximation-derived AOD is above EE, although this issue does not arise for SFART (only 14% of the values are above the EE).

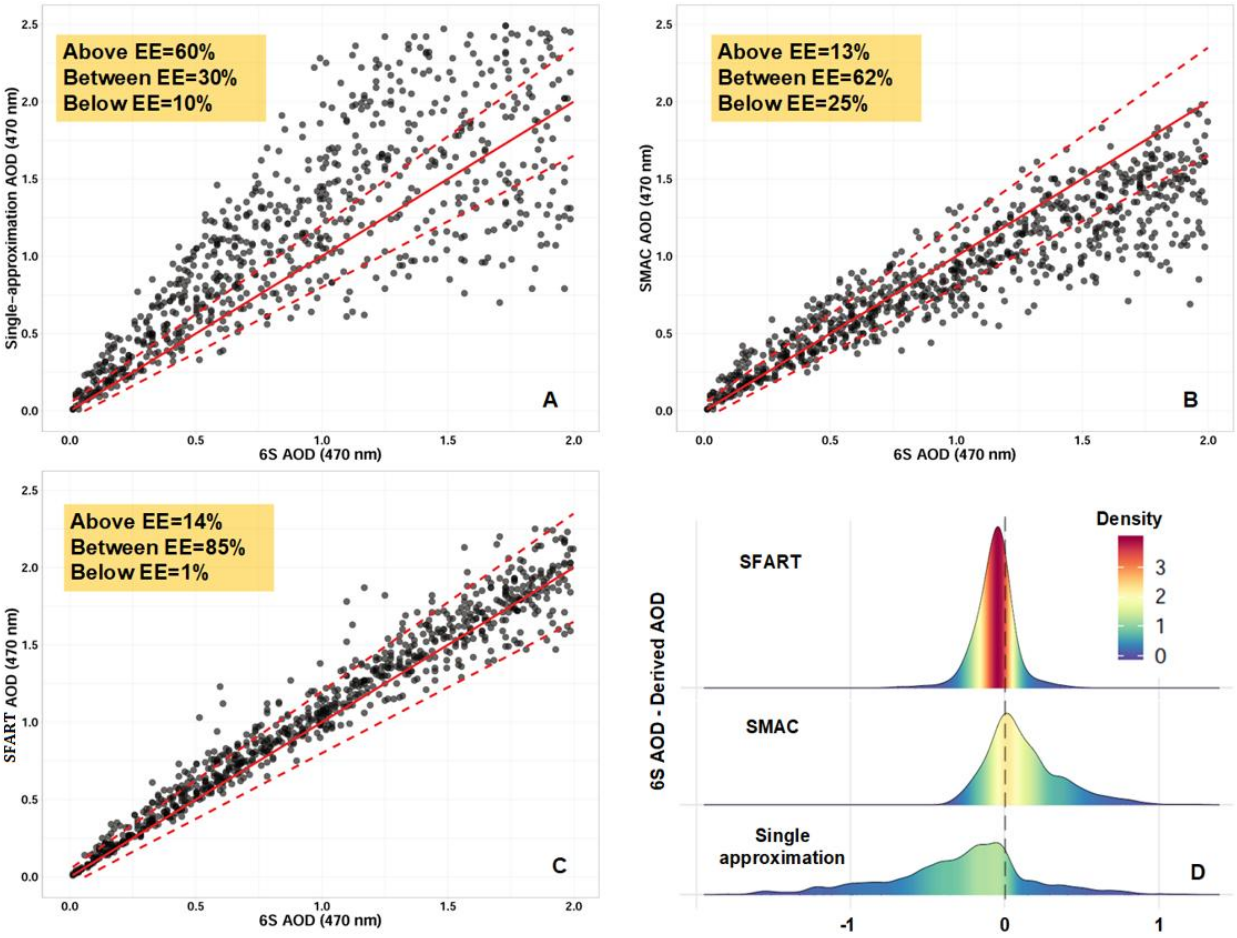

Figure 5. Single approximation-, SMAC- and SFART-derived AOD values compared with 6S at 470 nm (A, B and C). The two dashed error lines form the EE envelope ±(0.05 + 0.15 × 6S-derived AOD). The solid black line is the 1:1 line. D: Histogram of the derived AOD errors with 6S.

3.5 SFART application for Himawari-8 AOD retrieval

Aerosol retrieval over the North China Plain on 9 April 2018 is shown as an example in Figure 6. As reported by the China Meteorological Administration, 9 April 2018 is also a dust day in the Beijing region; the true color satellite image for the same day is shown in Figure S2A. On this day, high aerosol loading (0.8–1.2) was found in Beijing and Hebei (Figure 6A). Regarding the results for Tianjin shown in the figure, the retrieval values from SFART, MODIS Deep Blue (DB), and MODIS DT are similar (approximately 0.8), but Himawari-8 V2.1 provided lower values (approximately 0.6). In Figures 6A and B, there is a significant difference between the retrieved AOD values given by SFART and Himawari-8 V2.1 south of Hebei. As indicated by the red circle, high aerosol loading is indicated by SFART (0.8–1.2), which is similar to that determined from the MODIS DB and DT retrievals; however, the Himawari-8 V2.1 AOD values are only 0.4–0.6. In general, the SFART AOD spatial trend is consistent with those of MODIS DB and DT. Nevertheless, SFART exhibits superior spatial coverage to the MODIS products. Furthermore, although the day was cloud-free, many gaps are apparent in the MODIS DB and DT AOD retrievals east of Hebei and south of Shandong. The comparison of the SFART AOD with AERONET AOD is shown in Figure S2C. Although the SFART is underestimated in the CAMS and Xianghe AERONET location, the general accuracy is good for this dust day.

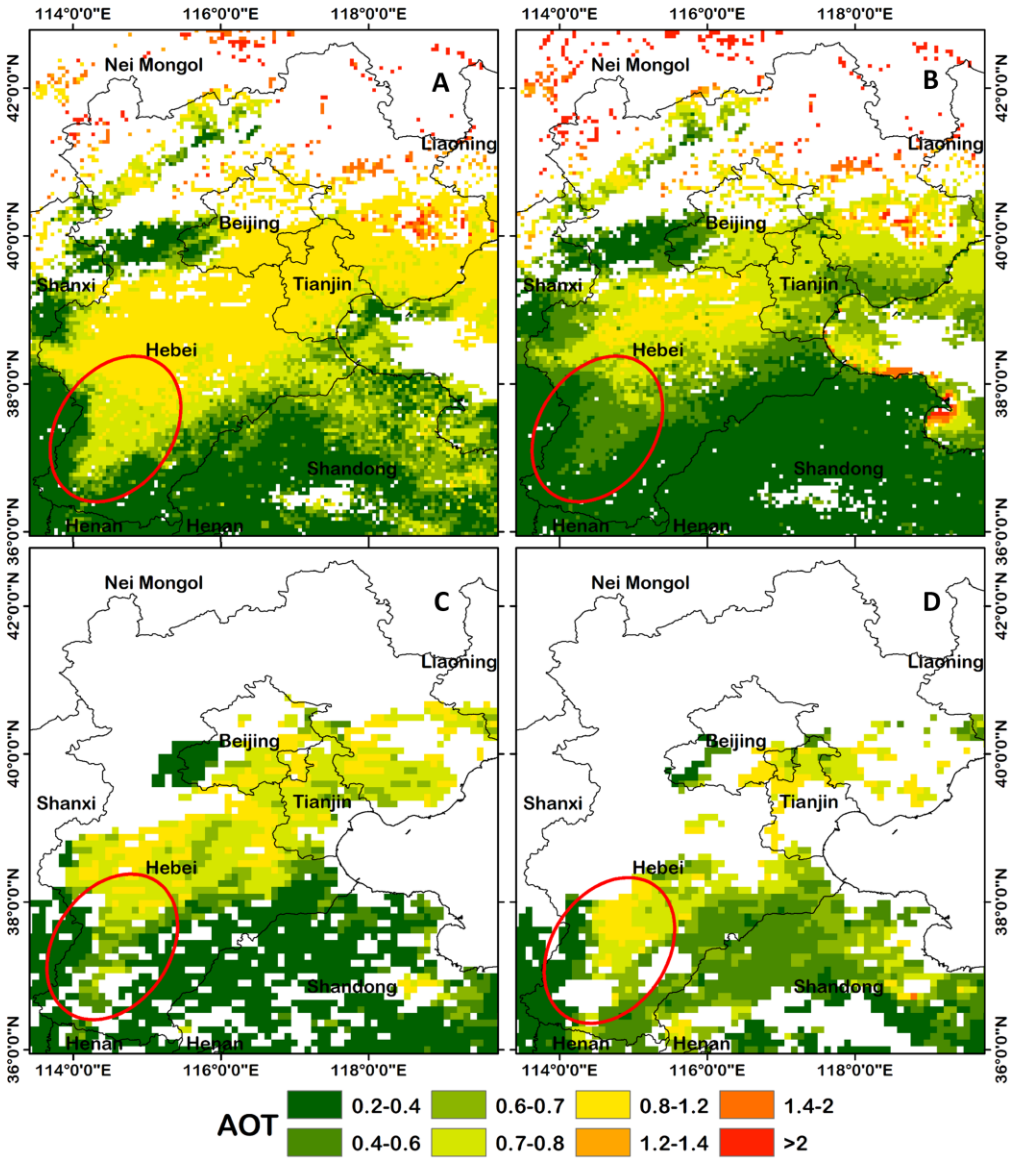

Figure 6. AOD spatial distributions over North China Plain given by (A) SFART, (B) Himawari-8 V2.1, (C) the MODIS DB algorithm, and (D) the MODIS DT algorithm on April 9, 2018. All the satellite images were obtained at 3:10 UTC.

3.6 SFART application on hazy day

Selection of different aerosol models can have a profound impact on final satellite AOD output (Liang et al., 2006), especially for hazy days (Li et al., 2013). Previously, Yan et al. (2016) developed an empirical haze aerosol model based on 12-year AERONET data to assist satellite haze aerosol retrieval. However, Li et al. (2013) have claimed that a dynamic day-based aerosol model may be more suitable for haze aerosol calculation. Although the asymmetry factor on a hazy day is similar to that on a normal day, there is a significant difference in SSA (Yan et al., 2016). AERONET collected data for Beijing are shown as an example in Figure S3. A significant daily variation of SSA can be found, with a mean SSA value of 0.92 for the whole year of 2018 and the maximum SSA reaching 0.99. To analyze the impact of SSA on AOD retrieval, box plots of absolute errors of derived AOD between using 6S continental aerosol model (SSA at 470 nm is 0.9) and real time SSA as a function of the SSA (0.7-1) were prepared, as shown in Figure S4. When the real time SSA value is close to that of the 6S continental aerosol model (between 0.85 and 0.95), the error of the derived AOD is always below 0.05 under the condition of AOD<0.5. However, the SSA has a significant impact on the AOD accuracy when the AOD is large. When 1 < AOD < 2, the 6S continental aerosol model SSA can lead to absolute errors >0.5 or >1 for derived AOD.

As for the haze day, Figure 7A shows a comparison of the SSA on hazy and clean days (AOD < 0.5) at Xianghe AERONET in 2018. The SSA values at both 440 and 675 nm under hazy conditions are much higher than those on the clean day. Over the North China Plain, haze aerosol is mainly composed of fine particles of anthropogenic sources (Li et al., 2013), which cause increased scattering and, thus, increased SSA values (Yan et al., 2008). Therefore, in this study, we used the intraday AERONET SSA and asymmetry factor as the aerosol model for the

hazy-day AOD calculation. Figure 7B shows an accuracy comparison with results obtained using the 6S continental aerosol model for hazy-day aerosol retrieval. The error of the 6S continental aerosol model result seems high (RMSE = 0.67) and significantly overestimated. The SSA at 550 nm for the 6S continental aerosol model is 0.89 (Bevan et al., 2012), which is much lower than the general SSA value under hazy conditions (Li et al., 2013). However, use of the intraday AERONET-based haze aerosol model yields an effective enhancement of the result precision (the RMSE decreases from 0.63 to 0.51), with the overestimation issue being obviously reduced.

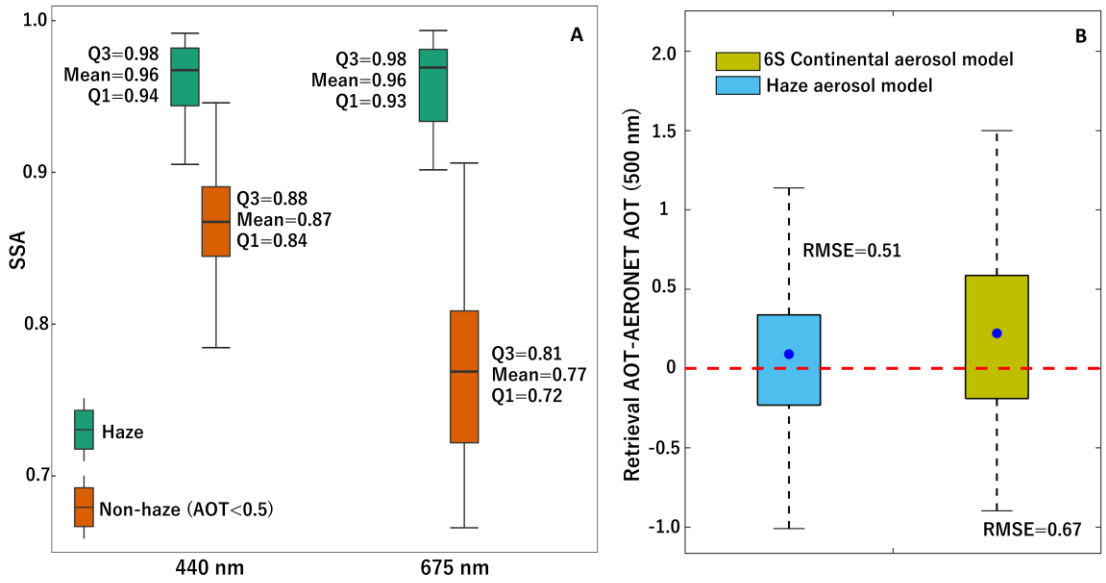

Figure 7. (A): Box plots of SSA between hazy and non-hazy conditions at 440 and 675 nm at Xianghe AERONET. (B): Box plots of AOD errors (retrieved AOD – AERONET AOD) at 500 nm using 6S continental aerosol model and haze aerosol model.

To illustrate the SFART performance on a hazy day, we used a retrieval result obtained over the North China Plain on 13 March 2018 as an example. A comparison of the SFART results

with the Himawari-8 V2.1, MODIS DB, and MODIS DT AOD products is shown in Figure 8. High AOD values (1.6–2.1) are evident between Tianjin, Tangshan, and Qinhuangdao (Figures 8A–C). The spatial trends of the SFART, Himawari-8 V2.1, and MODIS DB results exhibit good consistency. However, as indicated by the blue circle areas, the Himawari-8 V2.1 product seems to have overestimated the AOD compared with the SFART and MODIS DB results. In this region, the Himawari-8 V2.1 AOD values are higher than 2.1, but this level of AOD is not given by the SFART and MODIS DB methods. Further, the MODIS DT AOD product (Figure 8D) omits most values under hazy conditions; this limitation has also been reported by Li et al. (2013) and Yan et al. (2016). Note that this unsuccessful AOD retrieval by MODIS DT under the influence of hazy weather may cause underestimation of the haze aerosol loading (Tao et al., 2012).

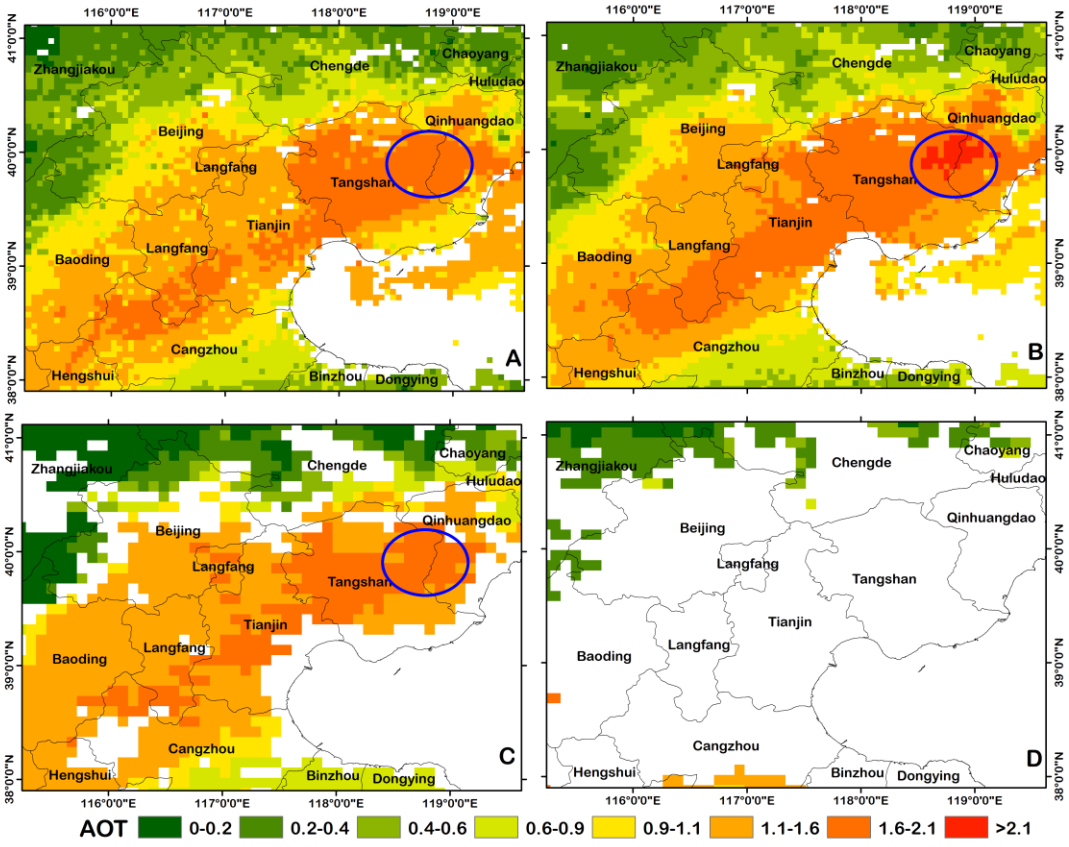

Figure 8. AOD distributions on hazy day (March 13, 2018): (A) SFART; (B) Himawari-8 V2.1; (C) MODIS DB algorithm; (D) MODIS DT algorithm.

3.7 Validation

To evaluate the SFART performance, the Himawari-8 5-km retrieved AOD was validated against products from three AERONET stations (Beijing, CAMS, and Xianghe) in the North China Plain. For further comparison, the most recent Himawari-8 V2.1 AOD at the same 5-km resolution was also compared with the AERONET data. In this validation, AERONET Version 3 Level 2.0 products were used. To focus on the fine-scale AOD, the single satellite pixel closest to the AERONET coordinates was used; this approach is identical to that used for the MAIAC AOD validation presented by Emili et al. (2011). As shown in Figure 9, 339 collocations for the year 2018 were matched. Linear regression of the SFART AOD against the AERONET measurements yielded an R^2 of 0.86, which is higher than the AOD obtained from the Himawari-8 V2.1 product (R^2 = 0.78). In the figure, the scatterplot of the SFART values tends to be concentrated closer to the 1:1 line, with 59% of the results falling within the EE envelope. However, for Himawari-8 V2.1, this value is only 48%. In addition, compared with Himawari-8 V2.1, the RMSE for SFART decreases from 0.33 to 0.22. From Figure 8B, it is apparent that more of the Himawari-8 V2.1 retrievals fall below the EE envelope (37%); however, this underestimation issue is improved for SFART (28%).

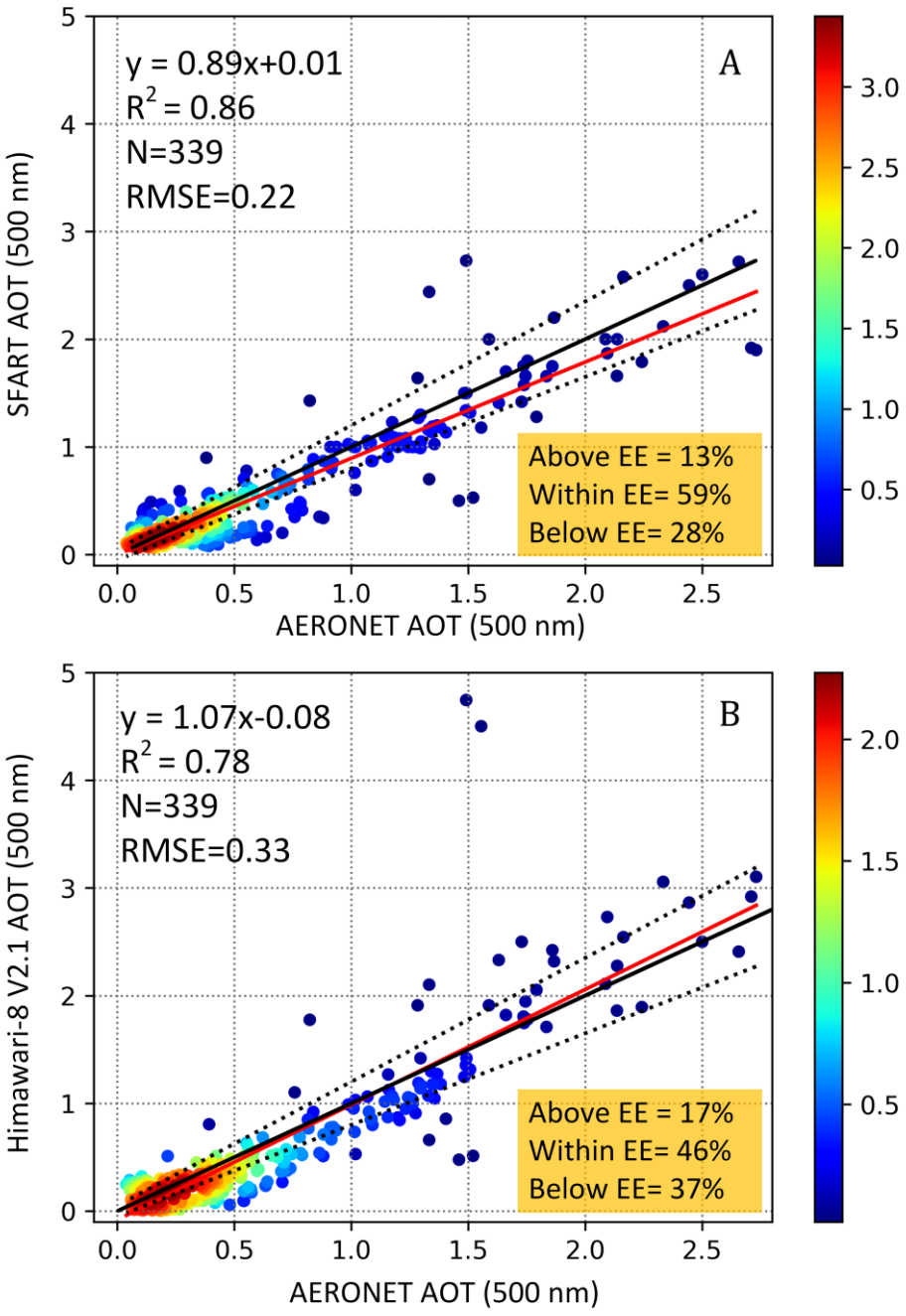

433

434 **Figure 9**. SFART and Himawari-8 V2.1 AOD results retrieved at 500 nm compared with
435 AERONET AOD values. The red solid line is the linear regression line, the two black dashed
436 lines given the EE for AOD ±(0.05 + 0.15) and the black solid line is the 1:1 line.

437

4 Discussion

The simplifications employed in SMAC accelerate the process, but at the cost of accuracy (Proud et al., 2010). Although SMAC has been successfully applied for atmospheric correction to data from the Medium Resolution Imaging Spectrometer (MERIS; Beal et al., 2003), the Satellite Pour l'Observation de la Terre (SPOT) (Maisongrande et al., 2004), and Formosat-2 (Hagolle et al., 2008), we encountered difficulties in applying SMAC for satellite AOD retrieval in this study. Because of the inaccuracies of the aerosol reflectance estimation (Figure 3) and the single Rayleigh reflectance approximation, the SMAC AOD output cannot match the 6S AOD well (Figure 5).

6S has been extensively validated to ensure its accuracy (Kotchenova et al., 2006). Of course, it is possible to directly run 6S for AOD calculation for each satellite pixel, as reported by Li et al. (2013); however, that approach would be very time consuming. According to Seidel et al. (2010), 6S requires approximately 1.4 s for one calculation; thus, it is unsuitable for pixel-by-pixel application to large images. Currently, the SFART calculation time is 97 s for 10,000 observations, which is approximately 140 times faster than 6S. Another feature of SFART is that it can directly employ real-time ground-based measurements to determine the aerosol model and assist AOD retrieval in the case of extreme weather. Thus, SFART is more convenient and flexible than the LUT-based method, for which the aerosol model used to create the table for a given time and space must be pre-defined (Liang et al., 2006). Further, pre-defined aerosol models do not usually represent, or struggle to represent, hazy conditions (Li, et al., 2013; Tao et al., 2012; Yan et al., 2016; Shang et al., 2017). Currently, the MODIS C6 DT algorithm (with 6S-based LUT) is always employed with the moderately (SSA = 0.90) or weakly absorbing (SSA = 0.95) aerosol model for the North China Plain (Levy et al., 2010). However, as shown in Figure 7, the SSA can exceed 0.98 on hazy days.

In the satellite AOD retrieval process, surface reflectance plays a key role in differentiating between signals from land and the atmosphere (Jiang et al., 2019; Choi et al., 2019). Zheng et al. (2011) indicated that inaccurate surface reflectance is a major source of error in satellite AOD calculation. Regarding the determination of surface reflectance Himawari-8 V2.1 only corrects Rayleigh scattering when surface reflectance is found as the second-lowest reflectance (Yoshida et al., 2018). Although this method can reduce the time cost of the Eq. (1) calculation (AOD = 0), the background AOD should not be neglected, especially for high-pollution areas, such as Xingtai in the south of Hebei, China. Background AOD reflectance may contribute to the overestimation of surface reflectance. In this study, the estimation of surface reflectance benefited from the fast SFART computation, with the impact of both the Rayleigh and background AOD scattering being considered.

As apparent from Figure 4 and Table 2, single scattering approximation for both Rayleigh and aerosol reflectance yields an extremely large error in the atmospheric reflectance estimation, especially for the blue band (440 nm). Previously, Antoine and Morel (1998) indicated that only τ_R and τ_a are sufficiently small (< 0.1) for the single scattering approximation to be applied. Thus, we do not recommend use of the single scattering assumption in the satellite AOD retrieval process if a high-accuracy result is desired.

5 Conclusions

In this study, we developed the SFART model for AOD retrieval from satellite data. We first compared the atmospheric reflectance from SFART with that from SMAC, a single-scattering approximation RTM, and 6S. A particularly high relative error was found for the single scattering approximation for the blue-band (440 nm) Rayleigh reflectance calculation at

large scattering angle (>140°) and solar and sensor zenith angles (>50°). This result indicates that the impact of multiple scattering on Rayleigh approximation should not be neglected, especially for the satellite short-wavelength band. Together with the Rayleigh and aerosol reflectance, the results given by SFART exhibited good agreement with 6S (approximately 69% of the data fell within the 5% EE at both 440 and 640 nm), which was a significant improvement over SMAC (within 5% EE: 42.83% and 39.91% at 440 and 640 nm, respectively) and single scattering approximation (within 5% EE: 15.67% and 20.5% at 440 and 640 nm, respectively) results. In addition, a significant underestimation of the atmospheric reflectance was found for the single scattering approximation method (below 5% EE: 76.98% and 75.12% at 440 and 640 nm, respectively). Therefore, we conclude that the single scattering approximation does not provide sufficient accuracy for many sets of atmospheric conditions, and should be used very carefully in the context of satellite AOD retrieval.

When applied to satellite images, SFART performs atmospheric correction and aerosol retrieval over both bright and dark surfaces (with the exception of snow). The high processing speeds of SFART are very useful when handling large images, such as geostationary Himawari-8 images with high spatial and temporal resolution. The SFART atmospheric correction is performed to determine surface reflectance, with the correction for both Rayleigh scattering and background aerosol scattering when surface reflectance is the second-lowest reflectance. In a validation with AERONET measurements, 59% of the SFART AOD values fell within the EE bounds of ±(0.05 + 15%) with an RMSE of 0.22 (N = 339). This result is superior to that for the Himawari-8 V2.1 AOD values (46% within EE, RMSE = 0.33). In addition, an underestimation issue was found for the Himawari-8 V2.1 AOD values, as 37% of the data points were below the EE. However, this underestimation was improved in the case of SFART (28% below the EE).

SFART uses an analytical equation to directly calculate the AOD without an LUT; thus, a real-time aerosol model can be employed in the retrieval process.

SFART uses an analytical equation to directly calculate the AOD without an LUT; thus, a real-time aerosol model can be employed in the retrieval process. This feature is very important for AOD calculation in the case of extreme weather, e.g., on hazy days. This study demonstrates that the SFART is an effective method to derive AOD for Himawari-8 data. In addition, the SFART can be further applied to other satellites, e.g., Landsat 8 or the Fenyun-4.

Acknowledgments

This work was supported by the National Natural Science Foundation of China (41801329, 91544217, 91837204), the National Key Research and Development Plan of China (2017YFC1501702), the Open Fund of State Key Laboratory of Remote Sensing Science (OFSLRSS201915) and the Fundamental Research Funds for the Central Universities. The authors gratefully acknowledge the MODIS and AERONET teams for their effort in making the data available. We would like to thank the Meteorological Satellite Center (MSC) of the Japan Meteorological Agency (JMA) for providing Himawari-8 data.

References

Anderson, J.O., Thundiyil, J.G., Stolbach, A., 2012. Clearing the air: a review of the effects of particulate matter air pollution on human health. J. Med. Toxicol. 8, 166-175.

Antoine, D., Morel, A., 1998. Relative importance of multiple scattering by air molecules and aerosols in forming the atmospheric path radiance in the visible and near infrared parts of the spectrum. Appl. Opt. 37 (12), 2245-2259.

Beal, D., F. Baret, M. Weiss, X. Gu, and M. Verbrugghe (2003), A method for MERIS atmospheric correction based on the spectral and spatial observation, Geoscience and Remote Sensing Symposium, 2003. IGARSS ’03. Proceedings, 6, 3601–3603.

Bellouin, N., Boucher, O., Haywood, J., Reddy, M.S., 2005. Global estimates of aerosol direct radiative forcing from satellite measurements. Nature 438, 1138-1141.

Berk, A., Bernstein, L. S., & Robertson, D. C. (1987). MODTRAN: A moderate resolution model for LOWTRAN (No. SSI-TR-124). SPECTRAL SCIENCES INC BURLINGTON MA.

Bessho, K., Date, K., Hayashi, M., Ikeda, A., Imai, T., Inoue, H., et al., 2016. An introduction to Himawari-8/9 - Japan's new-generation geostationary meteorological satellites. J. Meteorol. Soc. Japan Ser. II 94 (2), 151-183.

Bevan, S.L., North, P.R., Los, S.O., Grey, W.M., 2012. A global dataset of atmospheric aerosol optical depth and surface reflectance from AATSR. Remote Sens. Environ. 116, 199-210.

Bi, J., Belle, J. H., Wang, Y., Lyapustin, A. I., Wildani, A., & Liu, Y. (2019). Impacts of snow and cloud covers on satellite-derived PM2. 5 levels. Remote Sensing of Environment, 221, 665-674.

Bilal, M., Nichol, J.E., Bleiweiss, M.P., Dubois, D., 2013. A simplified high resolution MODIS Aerosol Retrieval Algorithm (SARA) for use over mixed surfaces. Remote Sens. Environ. 136, 135-145.

Choi, M., Lim, H., Kim, J., Lee, S., Eck, T. F., Holben, B. N., Garay, M. J., Hyer, E. J., Saide, P. E., and Liu, H., 2019: Validation, comparison, and integration of GOCI, AHI, MODIS, MISR, and VIIRS aerosol optical depth over East Asia during the 2016 KORUS-AQ campaign, Atmos. Meas. Tech., 12, 4619–464.

Emili, E., Lyapustin, A., Wang, Y., Popp, C., Korkin, S., Zebisch, M., Wunderle, S. & Petitta, M. (2011). High spatial resolution aerosol retrieval with MAIAC: Application to mountain regions. Journal of Geophysical Research: Atmospheres, 116(D23).

Gordon, H. R., and A. Morel, Remote Assessment of Ocean Color for Interpretation of Satellite Visible Imagery, A review, in Lecture Notes on Coastal and Estuarine Studies, 113 pp., Springer-Verlag, New York, 1983

Hagolle, O., G. Dedieu, B. Mougenot, V. Debaecker, B. Duchemin, and A. Meygret (2008), Correction of aerosol effects on multi- temporal images acquired with constant viewing angles: Application to Formosat- 2 images, Remote Sens. Environ., 112, 1689-1701.

Hansen, J.E., Travis, L.D., 1974. Light scattering in planetary atmospheres. Space Sci. Rev. 16 (4), 527-610.

Jiang, T.; Chen, B.; Chan, K.K.Y.; Xu, B., 2019: Himawari-8/AHI and MODIS Aerosol Optical Depths in China: Evaluation and Comparison. Remote Sens., 11, 1011.

Katsev, I. L., Prikhach, A. S., Zege, E. P., Ivanov, A. P., & Kokhanovsky, A. A. (2009). Iterative procedure for retrieval of spectral aerosol optical thickness and surface reflectance from satellite data using fast radiative transfer code and its application to MERIS measurements. In Satellite aerosol remote sensing over land (pp. 101-133). Springer, Berlin, Heidelberg.

Kaufman, Y. J., Tanré, D., & Boucher, O. (2002). A satellite view of aerosols in the climate system. Nature, 419(6903), 215.

Knapp, K.R., Frouin, R., Kondragunta, S., Prados, A., 2005. Toward aerosol optical depth retrievals over land from GOES visible radiances: determining surface reflectance. Int. J. Remote Sens. 26, 4097–4116.

Kokhanovsky, A. A., Mayer, B., & Rozanov, V. V. (2005). A parameterization of the diffuse transmittance and reflectance for aerosol remote sensing problems. Atmospheric Research, 73(1-2), 37-43.

Kotchenova, S., E. Vermote, R. Matarrese, and F. Klemm (2006), Validation of a vector version of the 6S radiative transfer code for atmospheric correction of satellite data. Part I: Path radiance, Appl. Opt., 45, 6762-6774.

Lee, C. S. , Yeom, J. M. , Lee, H. L. , Kim, J. J. , & Han, K. S. . (2015). Sensitivity analysis of 6s-based look-up table for surface reflectance retrieval. Asia-Pacific Journal of Atmospheric Sciences, 51(1), 91-101.

Lee, K.H., Kim, Y.J., 2010. Satellite remote sensing of Asian aerosols: a case study of clean, polluted and dust storm days. Atmos. Meas. Tech. Discuss. 3 (6), 1771-1784.

Letu, H., T. M. Nagao, T. Y. Nakajima J. Riedi, H. Ishimoto, A. J. Baran, H. Shang, M. Sekiguchi, and M. Kikuchi: Ice cloud properties from Himawari-8/AHI next-generation geostationary satellite: Capability of the AHI to monitor the DC cloud generation process.

IEEE Transactions on Geoscience and Remote Sensing, DOI: 10.1109/TGRS.2018.2882803.

Levy, R.C., Remer, L.A., Mattoo, S., Vermote, E.F., Kaufman, Y.J., 2007. Second-generation operational algorithm: retrieval of aerosol properties over land from inversion of moderate resolution imaging spectroradiometer spectral reflectance. J. Geophys. Res.-Atmos. 112, D13211.

Li, L., Zhang, J., Meng, X., Fang, Y., Ge, Y., Wang, J., Wang, C., Wu, J., & Kan, H. (2018). Estimation of PM2. 5 concentrations at a high spatiotemporal resolution using constrained mixed-effect bagging models with MAIAC aerosol optical depth. Remote Sensing of Environment, 217, 573-586.

Li, S., Chen, L., Xiong, X., Tao, J., Su, L., Han, D., Liu, Y., 2013. Retrieval of the haze optical thickness in North China Plain using MODIS data. IEEE Trans. Geosci. Remote Sens. 51 (5), 2528–2540.

Li, Z., Zhao, X., Kahn, R., Mishchenko, M., Remer, L.A., Lee, K.-H., Wang, M., Laszlo, I., Nakajima, T., Maring, H., 2009. Uncertainties in satellite remote sensing of aerosols and impact on monitoring its long-term trend: a review and perspective. Ann. Geophys. 27, 1-16.

Liang, S., Zhong, B., & Fang, H. (2006). Improved estimation of aerosol optical depth from MODIS imagery over land surfaces. Remote Sensing of Environment, 104(4), 416-425.

Lyapustin, A. , Wang, Y. , Korkin, S. , & Huang, D. . (2018). Modis collection 6 maiac algorithm. Atmospheric Measurement Techniques, 11(10), 5741-5765.

Lyapustin, A. , Wang, Y. , Laszlo, I. , Kahn, R. , Korkin, S. , & Remer, L. , et al. (2011b). Multiangle implementation of atmospheric correction (MAIAC): 2. aerosol algorithm. Journal of Geophysical Research Atmospheres, 116(D3).

Lyapustin, A. I. (2005). Radiative transfer code SHARM for atmospheric and terrestrial applications. Applied Optics, 44(36), 7764-7772.

Lyapustin, A., Martonchik, J., Wang, Y., Laszlo, I., & Korkin, S. (2011a). Multiangle implementation of atmospheric correction (MAIAC): 1. Radiative transfer basis and look-up tables. Journal of Geophysical Research: Atmospheres, 116(D3).

Maisongrande, P., B. Duchemin, and G. Dedieu (2004), VEGETATION/ SPOT: An operational mission for the Earth monitoring; presentation of new standard products, Int. J. Remote Sens., 25, 9-14.

Mei, L. L., Xue, Y., Kokhanovsky, A. A., von Hoyningen-Huene, W., de Leeuw, G., & Burrows, J. P. (2014). Retrieval of aerosol optical depth over land surfaces from AVHRR data. Atmospheric Measurement Techniques, 7(8), 2411-2420.

Munchak, L.A., Levy, R.C., Mattoo, S., Remer, L.A., 2013. MODIS 3 km aerosol product: applications over land in an urban/suburban region. Atmos. Meas. Tech. 6 (7), 1747-1759.

Patadia, F., Levy, R. C., & Mattoo, S. (2018). Correcting for trace gas absorption when retrieving aerosol optical depth from satellite observations of reflected shortwave radiation. Atmospheric Measurement Techniques, 11(6).

Proud, S. R., Fensholt, R., Rasmussen, M. O., & Sandholt, I. (2010). A comparison of the effectiveness of 6S and SMAC in correcting for atmospheric interference of Meteosat Second Generation images. Journal of Geophysical Research: Atmospheres, 115(D17).

Rahman, H., & Dedieu, G. (1994). SMAC: a simplified method for the atmospheric correction of satellite measurements in the solar spectrum. International journal of remote sensing, 15(1), 123-143.

Ramanathan, V., Crutzen, P.J., Kiehl, J.T., Rosenfeld, D., 2001. Aerosols, climate, and the hydrological cycle. Science 294, 2119-2124.

Remer, L.A., Kaufman, Y.J., Tanre, D., et al., 2005. The MODIS aerosol algorithm, products, and validation. J. Atmos. Sci. 62, 947-973.

Ricchiazzi, P., Yang, S.R., Gautier, C., Sowle, D., 1998. SBDART: a research and teaching software tool for plane-parallel radiative transfer in the Earth's atmosphere. Bull. Am. Meteorol. Soc. 79 (10), 2101–2114.

Riffler, M., Popp, C., Hauser, A., Fontana, F., & Wunderle, S. (2010). Validation of a modified AVHRR aerosol optical depth retrieval algorithm over Central Europe. Atmospheric Measurement Techniques, 3(5), 1255-1270.

Rozanov, A., Rozanov, V., Buchwitz, M., Kokhanovsky, A., & Burrows, J. P. (2005). SCIATRAN 2.0–A new radiative transfer model for geophysical applications in the 175–2400 nm spectral region. Advances in Space Research, 36(5), 1015-1019.

649 Seidel, F.C., Kokhanovsky, A.A., Schaepman, M.E., 2010. Fast and simple model for
650 atmospheric radiative transfer. Atmos. Meas. Tech. 3, 1129-1141.
651 Seidel, F.C., Kokhanovsky, A.A., Schaepman, M.E., 2012. Fast retrieval of aerosol optical depth
652 and its sensitivity to surface albedo using remote sensing data. Atmos. Res. 116 (8), 22-32.
653 Shang, H., Chen, L., Letu, H., Zhao, M., Li, S., & Bao, S. (2017). Development of a daytime
654 cloud and haze detection algorithm for Himawari- 8 satellite measurements over central
655 and eastern China. Journal of Geophysical Research: Atmospheres, 122(6), 3528-3543.
656 She, L., Mei, L., Xue, Y., Che, Y., & Guang, J. (2017). SAHARA: A simplified atmospheric
657 correction algorithm for Chinese GaoFen data: 1. Aerosol algorithm. Remote Sensing, 9(3),
658 253.
659 Shi, S., Cheng, T., Gu, X., Chen, H., Guo, H., Wang, Y., et al. (2017). Synergy of MODIS and
660 AATSR for better retrieval of aerosol optical depth and land surface directional
661 reflectance. Remote sensing of environment, 195, 130-141.
662 Tao, M.H., Chen, L.F., Su, L., Tao, J.H., 2012. Satellite observation of regional haze pollution
663 over the North China Plain. J. Geophys. Res.-Atmos. 117, D12203.
664 Tomasi, C., Fuzzi, S., & Kokhanovsky, A. (Eds.). (2017). Atmospheric Aerosols: Life cycles and
665 effects on air quality and climate (Vol. 1). John Wiley & Sons.
666 Vermote, E. F. T. D., Tanré, D., Deuzé, J. L., Herman, M., Morcrette, J. J., & Kotchenova, S. Y.
667 (2006). Second simulation of a satellite signal in the solar spectrum-vector (6SV). 6S User
668 Guide Version, 3, 1-55.
669 Vermote, E., & Tanre, D. (1992). Analytical expressions for radiative properties of planar
670 Rayleigh scattering media, including polarization contributions. Journal of Quantitative
671 Spectroscopy and Radiative Transfer, 47(4), 305-314.
672 Xin, J. , Gong, C. , Liu, Z. , Cong, Z. , Gao, W. , & Song, T. , et al. (2016). The observation-
673 based relationships between pm2.5 and aod over china. JOURNAL OF GEOPHYSICAL
674 RESEARCH-ATMOSPHERES, 121(18).
675 Yan, P., Tang, J., Huang, J., et al., 2008. The measurement of aerosol optical properties at a rural
676 site in Northern China. Atmos. Chem. Phys. 8, 2229-2242.
677 Yan, X., Li, Z., Luo, N., Shi, W., Zhao, W., Yang, X., & Jin, J. (2018). A minimum albedo
678 aerosol retrieval method for the new-generation geostationary meteorological satellite
679 Himawari-8. Atmospheric Research, 207, 14-27.

Yan, X., Shi, W., Luo, N., & Zhao, W. (2016). A new method of satellite-based haze aerosol monitoring over the North China Plain and a comparison with MODIS Collection 6 aerosol products. Atmospheric research, 171, 31-40.

Yoshida, M, M. Kikuchi, T. M. Nagao, H. Murakami, T. Nomaki, and A. Higurashi, 2018: Common retrieval of aerosol properties for imaging satellite sensors, J. Meteor. Soc. Japan, doi:10.2151/jmsj.2018-039.

Young, A. T. (1980). Revised depolarization corrections for atmospheric extinction. Applied Optics, 19(20), 3427-3428.

Zha, Y., Wang, Q., Yuan, J., Gao, Y., Jiang, J.J., Lu, H., Huang, J., 2011. Improved retrieval of aerosol optical thickness from MODIS measurements through derived surface reflectance over Nanjing, China. Tellus 58B, 952-958.

Zheng, Y., Dong, Z., Wu, R., Li, Z., Jiang, H., 2011. Validation of MODIS aerosol optical thickness retrieval over the Yangtze Delta region of China. Adv. Earth Science 26 (2), 224–234.